

# Masked Frequency Modeling for Self-Supervised Visual Pre-Training

Jiahao Xie<sup>1</sup>, Wei Li<sup>1</sup>, Xiaohang Zhan<sup>2</sup>, Ziwei Liu<sup>1</sup>, Yew Soon Ong<sup>1</sup>, Chen Change Loy<sup>1</sup>

<sup>1</sup>Nanyang Technological University <sup>2</sup>The Chinese University of Hong Kong  
{jiahao003, wei.l, ziwei.liu, asysong, ccloy}@ntu.edu.sg  
xiaohangzhan@outlook.com

## Abstract

We present **Masked Frequency Modeling (MFM)**, a unified frequency-domain-based approach for self-supervised pre-training of visual models. Instead of randomly inserting mask tokens to the input embeddings in the spatial domain, in this paper, we shift the perspective to the frequency domain. Specifically, MFM first masks out a portion of frequency components of the input image and then predicts the missing frequencies on the frequency spectrum. Our key insight is that predicting masked components in the frequency domain is more ideal to reveal underlying image patterns rather than predicting masked patches in the spatial domain, due to the heavy spatial redundancy. Our findings suggest that with the right configuration of *mask-and-predict* strategy, both the structural information within high-frequency components and the low-level statistics among low-frequency counterparts are useful in learning good representations. For the first time, MFM demonstrates that, for both ViT and CNN, a simple non-Siamese framework can learn meaningful representations even using **none** of the following: (i) extra data, (ii) extra model, (iii) mask token. Experimental results on ImageNet and several robustness benchmarks show the competitive performance and advanced robustness of MFM compared with recent masked image modeling approaches. Furthermore, we also comprehensively investigate the effectiveness of classical image restoration tasks for representation learning from a unified frequency perspective and reveal their intriguing relations with our MFM approach.<sup>1</sup>

## 1 Introduction

Following the success of Masked Language Modeling (MLM) such as BERT [17] in natural language processing (NLP), Masked Image Modeling (MIM) [1, 29, 68, 71] has shown promising performance in self-supervised pre-training of visual models. Both MLM and MIM follow a common *corrupt-and-predict* paradigm – randomly masking a portion of input data and then learning to predict the missing parts. This simple recipe enables modern Transformer-based deep architectures [63, 22] to learn generalizable representations from ubiquitous unlabeled text or image data.

By default, current MIM methods such as BEiT [1], MAE [29] and SimMIM [71] perform masking in the spatial domain by excluding image patches randomly, a strategy inspired by MLM that performs masking on words (Figure 1(a-b)). However, unlike human-generated language that is succinct and highly semantic, raw pixel values in the spatial domain are of low information density. To cope with heavy spatial redundancy in images, MAE [29] shows that one would need to mask a very high proportion (*e.g.*, 75%) to encourage the learning of meaningful features.

<sup>1</sup>Project page: <https://www.mmlab-ntu.com/project/mfm/index.html>

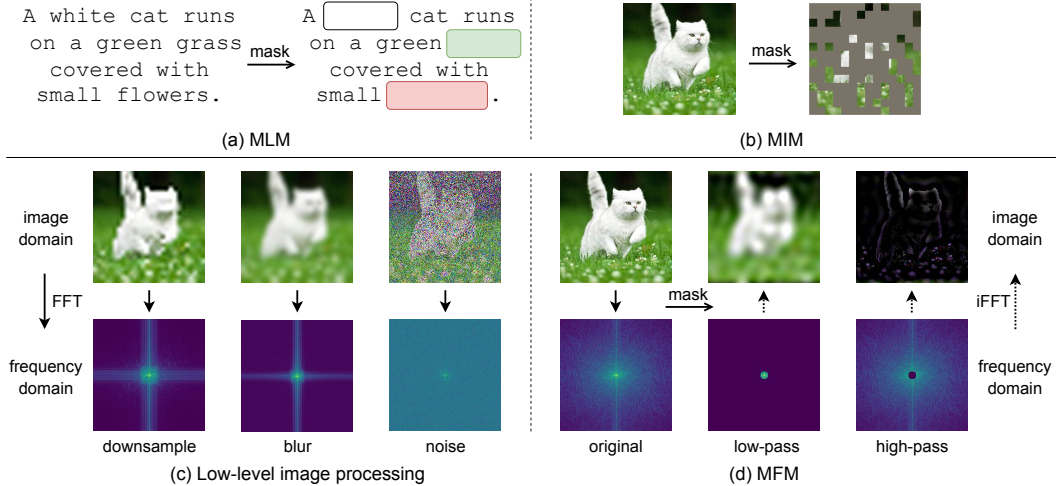


Figure 1: **Comparison of masking recipes** in Masked Language Modeling (MLM), Masked Image Modeling (MIM), low-level image processing and Masked Frequency Modeling (MFM). Note the differences of masked information among MIM, low-level image processing and MFM.

Beyond masking image patches, which is a particular way of corruption, in this paper, we are interested in investigating the effectiveness of other corruption strategies for self-supervised representation learning. We first explore the corruption recipes commonly applied in low-level image processing tasks, including image super-resolution (SR), deblurring and denoising. As shown in Figure 1(c), the downsampling, blur, and noise operations can degrade the exemplar image effectively in the spatial domain, thus potentially serving as useful corruption strategies. However, the corruption induced in the spatial domain prevents us from analyzing what specific information is corrupted and needs to be reconstructed. To better understand these low-level corruptions, we shift our attention from the spatial image domain to the frequency domain.

In the frequency domain, one could observe underlying patterns of an image not conveniently visible from raw pixel values. As values and locations are represented by sinusoidal relationships that depend on the frequency of a pixel occurring within an image, it becomes possible to determine which pixels contain more important information and whether repeating patterns occur. For example, the downsampling and blur operations dominantly remove the high-frequency image details, while adding noises tends to corrupt the full frequency spectrum of an image globally (Figure 1(c)).

Driven by this observation, we present a simple and effective masking strategy in the frequency domain for self-supervised visual representation learning, dubbed as **Masked Frequency Modeling (MFM)**. Specifically, we first perform Fast Fourier Transform (FFT) to convert each input image into its frequency representation, *i.e.*, frequency spectrum. We then mask a portion of frequencies on the frequency spectrum using a low-/high-pass filter. With inverse FFT (iFFT), we finally take the corrupted image with some of the frequencies attenuated as input. Our encoder is quite flexible as no mask tokens are inserted. Thus, MFM can embrace both the vision Transformer (ViT) [22] and convolutional neural network (CNN) [39] families. Our decoder is a lightweight linear layer that reconstructs the masked frequency values on the frequency spectrum via a frequency loss. As shown in Figure 1(d), an image with low or high frequencies attenuated would reveal entirely different patterns: the low-frequency components usually contain object smooth structure such as colors and styles, while the high-frequency counterparts largely depict the object outline or silhouette structure. Such unique properties of the frequency domain make it appealing for reducing information redundancy, thus creating a nontrivial and meaningful self-supervisory task.

Our contributions are summarized as follows:

**1)** We contribute the first study for self-supervised learning (SSL) in frequency domain. We investigate the effectiveness of corruption strategies commonly adopted in low-level image processing tasks (*i.e.*, SR, deblurring and denoising) for SSL from a frequency perspective and reveal that the representation learning capability of these corruption tasks actually depends on the architectures: when fine-tuned on ImageNet-1K [16], they can achieve comparable and even better results than their supervised counterpart on ViT, but no gains are observed on CNN.

2) We propose a new masked frequency modeling task to pre-train visual encoders in a self-supervised manner. Our MFM is agnostic to the architectures, and we demonstrate the flexibility of applying MFM for both ViT and CNN families.

3) Extensive experiments show that our MFM can achieve competitive performance among existing patch-based MIM approaches on standard ImageNet-1K classification benchmark, while not using mask tokens or other more complex designs. Further analysis on several robustness benchmarks also exhibits more appealing robustness of the studied corruption tasks than MIM.

## 2 Related Work

**Masked language modeling** and its auto-regressive variants, such as BERT [17] and GPT [54, 55, 5], have achieved great success in pre-training large-scale language models in the NLP community. These approaches perform masking on the human-generated language by holding out random words and then predicting the missing content. This simple *mask-word* recipe has shown excellent ability in pre-training generalizable representations for broad NLP applications.

**Masked image modeling** leverages images corrupted by masking to learn useful representations. Pioneered with stacked autoencoders [64] and context encoders [52] using CNNs, recent approaches [1, 29, 71, 68, 10] follow the *mask-word* strategy in NLP to randomly mask image patches in the spatial domain using the vision Transformers [22, 40]. Along with this *mask-patch* strategy, different types of prediction targets have been studied, including discrete tokens [1, 21], raw pixels [29, 71], and hand-crafted features [68]. Besides, iGPT [8] takes a low-resolution image sequence as input and predicts missing pixels in an auto-regressive manner. Several methods [79, 23] also integrate MIM into contrastive-based Siamese frameworks. Our work differs from previous approaches in that we perform masking in the frequency domain, which relies on *none* of the following: (i) extra data [1, 21, 24], (ii) extra model [79, 23, 24, 57, 10], or (iii) mask token [1, 29, 71, 68, 10]. Concurrently, CIM [24] also does not use mask token. However, introducing an auxiliary generator to corrupt the input images adds nontrivial pre-training overhead. In contrast, our frequency-domain-based corruption strategy can achieve comparable performance with negligible computational cost.

**Self-supervised learning** mainly focuses on designing effective pretext tasks for pre-training [18, 66, 44, 38, 77, 78, 45, 4, 51, 25]. Contrastive learning [70, 30, 43, 9, 11, 27, 12, 13, 7] has dominated the field over the past few years. Unlike the *mask-and-predict* pretext task, contrastive learning typically uses a Siamese framework and greatly relies on data augmentation.

**Low-level image processing** tasks, such as image super-resolution [20], deblurring [75] and denoising [76], focus on restoring the high-fidelity image from its corrupted input. The corrupted images are usually generated with degradation transformations, which consist of downsampling, blur, noise and JPEG compression. Recent promising results of MIM motivate us to investigate the effectiveness of these corruption operations in the context of representation learning.

**Frequency domain analysis** has been widely adopted in many computer vision tasks, such as image generation [37], domain adaptation [72], and image super-resolution [49]. Early studies [47, 48, 53, 28] have revealed that in the frequency domain, the phase component largely captures high-level semantics of the original signals, while the amplitude component mainly retains low-level statistics. As such, underlying image patterns can be more conveniently observed in the frequency representation, compared with the raw pixel values in the spatial domain. Motivated by the intriguing properties of the Fourier domain, we propose a novel *mask-frequency* recipe and conduct *the first study w.r.t.* masked information modeling in the frequency domain for image data.

## 3 Approach

Our masked frequency modeling (MFM) is a simple yet effective self-supervised pre-training approach, which masks out a portion of image frequency components and predicts the missing frequencies on the frequency spectrum. Figure 2 shows the overview of our approach. The framework consists of four components: masking strategy, encoder, decoder, and reconstruction target. In the following subsections, we first introduce the frequency representation of images in Section 3.1. We then detail each component of MFM in Section 3.2. We finally discuss the relation of our approach with low-level image processing tasks in Section 3.3.

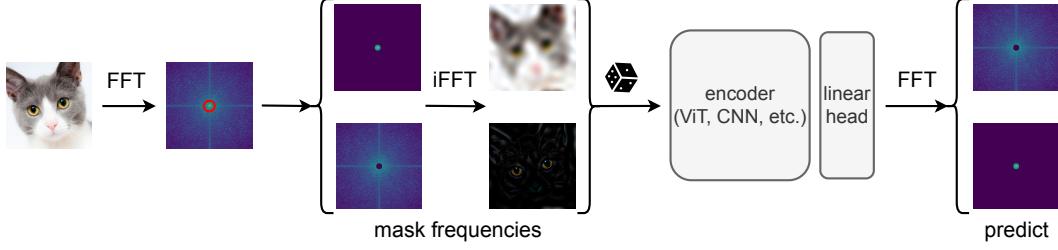


Figure 2: **Overview of our MFM pre-training pipeline.** We convert each input image into frequency domain via FFT and mask a portion of frequencies on the frequency spectrum via a low-/high-pass filter. After iFFT, the low-/high-pass filtered images are then randomly fed to the encoder (*e.g.*, ViT, CNN), with a lightweight one-layer head to predict the masked frequency values on the frequency spectrum via a frequency loss. The dice icon refers to the random sampling process of low-/high-pass filters, following a Bernoulli distribution.

### 3.1 Preliminary: Frequency Representation of Images

Given a single channel image  $x \in \mathbb{R}^{H \times W}$ , we can obtain the corresponding frequency representation via 2D Discrete Fourier Transform  $\mathcal{F}(x)$ :

$$\mathcal{F}(x)(u, v) = \sum_{h=0}^{H-1} \sum_{w=0}^{W-1} x(h, w) e^{-i2\pi(\frac{uh}{H} + \frac{vw}{W})}, \quad (1)$$

where  $x(h, w)$  is the real pixel value at the coordinate of  $(h, w)$  on the spatial image,  $\mathcal{F}(x)(u, v)$  is the complex frequency value at the coordinate of  $(u, v)$  on the frequency spectrum,  $e$  and  $i$  are Euler's number and the imaginary unit, respectively.

Let  $\mathcal{R}(x)$  and  $\mathcal{I}(x)$  be the real and imaginary part of  $\mathcal{F}(x)$ , respectively. The amplitude and phase components of a complex frequency value can be respectively expressed as:

$$\begin{aligned} \mathcal{A}(x)(u, v) &= \left( \mathcal{R}(x)(u, v)^2 + \mathcal{I}(x)(u, v)^2 \right)^{1/2}, \\ \mathcal{P}(x)(u, v) &= \arctan \left( \frac{\mathcal{I}(x)(u, v)}{\mathcal{R}(x)(u, v)} \right). \end{aligned} \quad (2)$$

Accordingly,  $\mathcal{F}^{-1}(x)$  defines the inverse Fourier transform that maps spectral signals back into original image space. Both the Fourier transform and its inverse can be calculated efficiently using the FFT algorithm [46]. For RGB images, the procedure is operated on each channel independently.

### 3.2 Masked Frequency Modeling

**Masking strategy.** We define a mask  $M \in \{0, 1\}^{H \times W}$ , whose value is determined by a thresholding function that separates the low and high frequency components from  $\mathcal{F}(x)$  according to a hyper-parameter, *i.e.*, radius  $r$ :

$$M(u, v) = \begin{cases} 1, & \text{if } d((u, v), (c_h, c_w)) < r \\ 0, & \text{otherwise} \end{cases} \quad (3)$$

where  $(c_h, c_w)$  denotes the center of the image,  $d(\cdot, \cdot)$  denotes a certain distance criterion. Here, we use the Euclidean distance, *i.e.*, a circle mask as default. Note that the mask shape is not solely restricted to a circle one, and we study the effects of different mask shapes in the experiment section.

With the predefined mask  $M$ , we can easily obtain the decomposed low-pass filtered image  $x_l$  and the high-pass filtered counterpart  $x_h$  as follows:

$$x_l = \mathcal{F}^{-1}(\mathcal{F}(x) \odot M), \quad x_h = \mathcal{F}^{-1}(\mathcal{F}(x) \odot (\mathbb{I} - M)), \quad (4)$$

where  $\mathbb{I}$  is the identity matrix,  $\odot$  is the Hadamard product between matrices. These filtered images are then randomly selected and fed to an encoder as input, following a Bernoulli distribution. Note that despite performing masking in the frequency domain, we still take the converted spatial images as input such that our model would not suffer an input domain gap between pre-training and fine-tuning.



**MFM encoder.** The architecture of our encoder is quite flexible since we do not insert any mask tokens on the corrupted non-overlapping patch embeddings as in MIM [1, 29, 71, 68]. Therefore, our MFM can be applied on both ViT and CNN architectures without any special designs. In this paper, we mainly use a standard ViT [22] as our encoder for a direct comparison with MIM methods. Specifically, we first divide a filtered image into regular non-overlapping patches. Then, the encoder embeds the patches by linear projection with added positional embeddings. The combined embeddings are then processed via a series of self-attention-based Transformer blocks [63]. We also consider a typical CNN architecture, *i.e.*, ResNet-50 [31], to demonstrate the versatility of MFM. To this end, we simply send the filtered image to the CNN encoder as input.

**MFM decoder.** The decoder accomplishes the frequency reconstruction task. It can be of arbitrary form as long as its input is compatible with the encoder’s output. The behaviors of different decoder architectures are beyond the focus of this study. Here, we simply adopt a lightweight linear layer as our decoder for efficiency. Note that the decoder is only employed during pre-training and is removed for downstream tasks.

**Reconstruction target.** Our MFM reconstructs the input by predicting the missing frequency values on the frequency spectrum. To faithfully recover the frequency values, we should define a frequency distance metric that considers both amplitude and phase as a loss function. Regarding each frequency value  $\mathcal{F}(x)(u, v)$  as a two-dimensional Euclidean vector  $\vec{f}$ , one can easily derive that the magnitude of the vector corresponds to the amplitude while the angle corresponds to the phase. Following the focal frequency loss [37], we thus define the frequency distance  $\mathcal{D}(\cdot, \cdot)$  as the distance between the reconstructed vector  $\vec{f}_r$  and the original vector  $\vec{f}_o$  at each spectrum coordinate  $(u, v)$ :

$$\begin{aligned} \mathcal{D}(\vec{f}_r, \vec{f}_o) &= \left\| \vec{f}_r - \vec{f}_o \right\|_2^\gamma = |\mathcal{F}_r(x)(u, v) - \mathcal{F}_o(x)(u, v)|^\gamma \\ &= ((\mathcal{R}_r(x)(u, v) - \mathcal{R}_o(x)(u, v))^2 + (\mathcal{I}_r(x)(u, v) - \mathcal{I}_o(x)(u, v))^2)^{\gamma/2}, \end{aligned} \quad (5)$$

where  $\gamma$  is an exponent to control the sharpness of the distance function and is set to 1 by default. For each image, the final loss function, *i.e.*, the average frequency distance of all spectrum positions can thus be written as:

$$\mathcal{L} = \mathcal{D}(\mathcal{F}_r(x), \mathcal{F}_o(x)) = \frac{1}{HW} \sum_{u=0}^{H-1} \sum_{v=0}^{W-1} |\mathcal{F}_r(x)(u, v) - \mathcal{F}_o(x)(u, v)|^\gamma. \quad (6)$$

In practice, we compute the loss only on the masked area of the frequency spectrum instead of the full spectrum as the latter tends to decrease the accuracy according to our experiments.

### 3.3 Relation with Low-Level Image Processing Tasks

The notion of recovering masked frequency components in MFM is reminiscent to the objectives in low-level image processing tasks, such as image super-resolution (SR), deblurring and denoising. In these tasks, a model takes a degraded image as input, and the aim is to restore the missing components. Different degradations corrupt different components in the frequency domain. As discussed in Section 1, for the image SR and deblurring tasks, most of the high-frequency components are removed while the low-frequency counterparts are retained; for the image denoising task, both low- and high-frequencies are significantly altered.

By analyzing the frequency spectrum of these tasks, we can observe how different frequencies of an image contribute to visual representation learning, thus gaining better insights on designing more effective learning objectives. Compared with these tasks, our MFM provides a more general and unified frequency perspective to perform these low-level corruptions while being conceptually simpler: we directly remove certain frequencies on the frequency spectrum via a low-/high-pass filter. Our experiments show that MFM can achieve better performance than these tasks for representation learning. We will comprehensively study these tasks and show more details in the experiment section.

## 4 Experiments

### 4.1 Implementation Details

We use the vanilla ViT-Small (ViT-S/16), ViT-Base (ViT-B/16) and ResNet-50 models as the backbones in our study. We perform self-supervised pre-training on the ImageNet-1K [16] training set

Table 1: **Ablations for MFM** with ViT-B/16 on ImageNet-1K. All models are based on 300-epoch pre-training, and we report top-1 fine-tuning accuracy. Unless specified, the default settings are: the mask type is random (*i.e.*, random sampling of low-/high-pass filters), the mask radius is 16, the mask shape is circle, the sampling ratio for low-pass filters is 50% (*i.e.*, 50% for low-pass filters and 50% for high-pass counterparts), the reconstruction target is masked frequencies on the spectrum, and the loss function is a frequency loss with  $\gamma = 1$ . Default entry is marked in gray.

(a) **Mask type.** Random sampling of both filters works the best.

Mask type	Top-1 acc (%)
none	76.5
low-pass	82.4
high-pass	82.3
random	<b>83.1</b>

(b) **Mask radius.** Using a fixed radius is enough.

Mask radius	Top-1 acc (%)
8	82.8
16	<b>83.1</b>
24	82.7
32	82.6
[8, 24]	83.0

(c) **Mask shape.** A circle mask is more accurate.

Mask shape	Top-1 acc (%)
circle	<b>83.1</b>
square	82.9
rhombus	82.8

(d) **Sampling ratio.** Sampling low-/high-pass filters with an equal probability is effective.

Sampling ratio	Top-1 acc (%)
0.3	82.5
0.5	<b>83.1</b>
0.7	82.7

(e) **Reconstruction target.** Predicting only the masked frequencies yields better performance.

Reconstruction target	Top-1 acc (%)
masked spectrum	<b>83.1</b>
full spectrum	82.4

(f) **Loss function.** A frequency loss works better than spatial loss.

Loss	Top-1 acc (%)
freq. ( $\gamma = 1$ )	<b>83.1</b>
freq. ( $\gamma = 2$ )	82.5
$\ell_1$	82.3
$\ell_2$	82.2

without labels. For ViT, our pre-training setting generally follows BEiT [1], while we simply use random resized cropping ( $224 \times 224$  resolution) and flipping as data augmentation, with dropout and stochastic depth not applied. We also do not use relative position or layer scaling. After pre-training, we conduct supervised end-to-end fine-tuning on ImageNet-1K image classification to evaluate the quality of learned representations, following BEiT [1]. The fine-tuning hyper-parameters mostly follow BEiT [1], while we set the layer-wise learning rate decay rate to 0.8 as suggested in [14]. For ResNet-50, we adopt the *same* pre-training configuration as that in ViT without further parameter tuning. We provide the detailed pre-training and fine-tuning recipes in the appendix.

## 4.2 Main Properties

We start by ablating our MFM using ViT-B/16 as the default backbone. All experiments are conducted with 300-epoch pre-training and 100-epoch fine-tuning on the ImageNet-1K dataset unless otherwise specified. Several intriguing properties are observed.

**Masking strategy.** We first study how different masking strategies on the frequency spectrum affect the effectiveness of representation learning. We consider two kinds of filters: low-pass filter (*i.e.*, mask high frequencies), and high-pass filter (*i.e.*, mask low frequencies). As shown in Table 1a, masking and predicting either high frequencies (“low-pass” entry) or low frequencies (“high-pass” entry) perform significantly better than simply encoding and reconstructing the original image (“none” entry). This indicates that both high-frequency and low-frequency components are useful in representation learning, where the former largely depicts the object structure information such as outline or silhouette and the latter usually captures low-level statistics such as colors and styles. A hybrid variant, *i.e.*, randomly selecting one filter from both low-pass and high-pass filters (“random” entry), benefits from all lens of frequencies, thus further improving the performance.

**Mask radius.** Table 1b studies the effect of mask radius, which controls the difficulty of our task. A larger radius leaves more frequencies for a low-pass filter while removes more frequencies for a high-pass filter. Our MFM works the best with a moderate difficulty. Using a fixed radius (*e.g.*, 16) performs slightly better than a random one, *i.e.*, the radius is uniformly sampled within a range (*e.g.*, [8, 24]).

**Mask shape.** We study three centrosymmetric mask shapes in Table 1c. Different mask shapes focus on different masking directions. Take low-pass filter as an example, a square shape removes more frequencies in the horizontal and vertical direction, while a rhombus one removes more in the

Table 2: **Comparison of SR, deblurring, denoising and MFM tasks** with ViT-B/16 on ImageNet-1K. All models are pre-trained for 300 epochs, and evaluated with top-1 fine-tuning accuracy. Corrupted image samples from ImageNet-1K training set with different degradation levels are visualized in both image and frequency domain. The studied hyper-parameter that controls the difficulty of degradation for each task is (a) downsampling scale factor, (b) Gaussian blur sigma, (c) Gaussian noise sigma, and (d) mask radius, respectively. More examples are provided in the appendix. Zoom in for best view.

Task	Parameter	Top-1 acc (%)
(a) SR	$\times 2$	82.1
	$\times 4$	82.2
	$\times 8$	<b>82.4</b>
	$\times 16$	82.1
(b) Deblur	1	79.7
	3	81.2
	5	<b>81.7</b>
	7	81.5
(c) Denoise	25	82.4
	50	82.6
	75	<b>82.7</b>
	100	82.6
(d) MFM	8	82.8
	16	<b>83.1</b>
	24	82.7
	32	82.6

diagonal direction. The results demonstrate that a circle mask shape that pays an equal attention to each direction on the frequency spectrum performs the best. We hypothesize that the effect of different mask shapes is largely correlated with the category statistics of pre-training datasets.

**Sampling ratio.** Table 1d ablates different sampling ratios for low-/high-pass filters. Here, the sampling ratio denotes the probability of sampling a low-pass filter, following a Bernoulli distribution. The results show that simply sampling both filters with an equal probability works the best.

**Reconstruction target.** Table 1e compares two reconstruction targets: 1) predicting *only* the masked frequencies on the frequency spectrum as in our default setting, and 2) recovering *both* the masked and unmasked frequencies on the frequency spectrum. Predicting the masked spectrum performs better than reconstructing the full spectrum by a clear margin (83.1% vs. 82.4%). This suggests that predicting the *invisible* signals is a more favourable task in representation learning, which is in accordance with the observation in recent MIM approaches.

**Loss function.** Table 1f studies the design of loss functions. A frequency loss performs better than a spatial loss (with  $\gamma = 1$  working the best). It makes sense as directly predicting the missing frequencies in the frequency domain better aligns to our MFM task.

### 4.3 Diagnosis of Low-Level Image Processing Tasks

In this subsection, we study the representation learning capability of low-level image processing tasks from a unified frequency perspective. We examine three representative tasks: image super-resolution (SR), deblurring, and denoising.

**Setup.** To ensure a direct comparison, we adopt the same pre-training and fine-tuning hyper-parameters as MFM and only alter the types of image degradation during pre-training. Specifically, for the SR task, we first use its standard data pre-processing, *i.e.*, bicubic downsampling, to downsample the input images by a scale factor. We then upsample them back to the original input size, *i.e.*,  $224 \times 224$ . For the deblurring task, we consider the commonly-used isotropic Gaussian filter and uniformly select the blur kernel size from  $\{7, 9, 11, 13, 15, 17, 19, 21\}$  as suggested in [67]. For the denoising task, we employ the typical Gaussian noise. The intensity of both deblurring and denoising tasks is controlled by the standard deviation (*i.e.*, sigma value) of the Gaussian distribution. For all tasks, the reconstruction target is the original image but in the frequency domain via the same frequency loss as MFM.

**Observations.** Table 2 shows the results with different levels of degradation for each task. We first notice that the optimal degradation level of each task in the context of representation learning is much heavier than its original task setting. For instance, a standard SR task usually has a

downsampling factor within  $\times 4$ , while we show that a much heavier  $\times 8$  setting works the best. With right configuration of the task difficulty, all these tasks can achieve comparable or even better performance than their supervised counterpart (*e.g.*, 81.8% in [60]), indicating that these low-level tasks are more or less helpful in representation learning. In addition, we observe that representation learning benefits from all lens of frequencies. This can be verified by the superior performance of denoising over SR and deblurring. As visualized in the frequency spectrum of the example image, denoising tends to intensify all frequencies of the spectrum, while SR and deblurring only removes high-frequency components. Thus, the performance of denoising is much closer to MFM, as both utilize the full frequency spectrum. Attenuating and intensifying frequencies on the spectrum are essentially two different ways of performing corruption in the frequency domain. We believe other corruption types may also work well and leave this exploration for future work.

#### 4.4 Comparison with Previous Methods

**ViT.** In Table 3, we compare the ImageNet-1K end-to-end fine-tuning results of self-supervised ViT-S/16 and ViT-B/16 models. We fine-tune ViT-S/16 for 200 epochs, and ViT-B/16 for 100 epochs. Other self-supervised models use the same or longer fine-tuning schedule. Compared with other representative self-supervised learners, our MFM can achieve comparable performance with fewer pre-training epochs while using *none* of the following: (i) extra data, (ii) extra model, (iii) mask token. This demonstrates the great potential of masked frequency modeling.

Table 3: ImageNet-1K top-1 fine-tuning accuracy of self-supervised models using ViT-S/16 and ViT-B/16 as the encoder. DINO and MoCo v3 use extra momentum encoder. BEiT requires extra 250M DALL-E data [56] to pre-train dVAE. BEiT and MAE also use mask tokens (inserted either in the encoder or the decoder). All entries are on an image size of  $224 \times 224$ . We use the actual processed images/views to measure the effective pre-training epochs [79]. Scratch indicates the supervised baseline in [60].  $^\dagger$ : doubled attention heads.  $^\ddagger$ : our re-implementation with official code.

Method	Pre-train data	Extra model	Mask token	Epochs	ViT-S	ViT-B
Scratch [60]	-	-	-	-	79.9	81.8
MoCo v3 [13]	IN-1K	momentum ViT	-	600	81.4 $^\dagger$	83.2
DINO [7]	IN-1K	momentum ViT	-	1600	81.5	82.8
BEiT [1]	IN-1K+DALL-E	dVAE	✓	300	81.3	82.9
MAE [29]	IN-1K	-	✓	300	80.6 $^\ddagger$	82.9 $^\ddagger$
SR	IN-1K	-	-	300	80.8	82.4
Deblur	IN-1K	-	-	300	79.4	81.7
Denoise	IN-1K	-	-	300	81.1	82.7
MFM	IN-1K	-	-	300	81.6	83.1

Table 4: ImageNet-1K top-1 fine-tuning accuracy of self-supervised models using ResNet-50 as the encoder. Table is split to three sub-tables for better placement. The results for other methods are taken from [24] as we adopt the same fine-tuning recipe.  $^\dagger$ : modified ResNet-50 architecture.

(a) Training-from-scratch baselines.			(b) Fine-tuning for 100 epochs.			(c) Fine-tuning for 300 epochs.		
Method	Epochs	Top-1 acc (%)	Method	Epochs	Top-1 acc (%)	Method	Epochs	Top-1 acc (%)
Original <sub>90</sub> [31]	-	75.3	RSB A3 [69]	-	78.1	RSB A2 [69]	-	79.8
PyTorch <sub>90</sub> [50]	-	76.1	SR	300	77.9	SimSiam [12]	400	79.1
FixRes <sub>120</sub> [62]	-	77.0	Deblur	300	78.0	MoCo v2 [11]	400	79.6
DeiT <sub>300</sub> [60]	-	78.4	Denoise	300	77.5	SimCLR [9]	800	79.9
ResNet-RS <sub>350</sub> $^\dagger$ [2]	-	78.8	MFM	300	78.5	BYOL [27]	400	80.0
FAMS <sub>400</sub> [19]	-	79.5				SwAV [6]	600	80.1
						MFM	300	80.1

**ResNet-50.** We demonstrate that MFM can also pre-train a high-capacity ResNet-50 model. We simply adopt the same pre-training settings as ViT. During fine-tuning, we generally follow the advanced vanilla ResNet “training from scratch” recipe in RSB [69] except that we use the AdamW optimizer [41] following [24]. Table 4 shows the results. Different from ViT, we observe performance degeneration of low-level image processing tasks like SR, deblurring and denoising compared with the RSB training-from-scratch baseline (Table 4b). We hypothesize this discrepancy is due to the architectural difference between ViT and CNN. Compared with ViT, the convolution operation in CNN tends to be more effective in capturing high-frequency components. Thus, encouraging a CNN model

Table 5: **Robustness evaluation on six robustness benchmarks.** We report top-1 accuracy of ViT-B/16 (*left*) and ResNet-50 (*right*) models except for IN-C that uses the mean corruption error (mCE). The original ImageNet top-1 fine-tuning results are also appended for reference. The best results are in **bold**, and the second best results are underlined.

Method	Robustness benchmarks						Orig.
	FGSM	PGD	IN-C ( $\downarrow$ )	IN-A	IN-R	IN-SK	
Scratch [60]	46.3	21.2	48.5	28.1	44.7	32.0	81.8
MAE [29]	38.9	11.2	52.3	<u>31.5</u>	48.3	33.8	<u>82.9</u>
SR	46.1	21.5	<b>46.3</b>	29.1	<b>49.2</b>	<b>35.5</b>	82.4
Deblur	42.5	17.2	49.2	25.3	46.9	33.2	81.7
Denoise	<u>47.6</u>	<u>24.3</u>	47.8	30.7	48.4	<u>34.8</u>	82.7
MFM	<b>47.7</b>	<b>24.4</b>	<u>47.5</u>	<b>32.7</b>	<u>48.6</u>	<u>34.8</u>	<b>83.1</b>

Method	Robustness benchmarks						Orig.
	FGSM	PGD	IN-C ( $\downarrow$ )	IN-A	IN-R	IN-SK	
Scratch [69]	<b>20.2</b>	<b>3.4</b>	77.0	6.6	36.0	25.0	<u>78.1</u>
SR	17.2	1.9	<b>73.6</b>	6.5	35.8	25.4	77.9
Deblur	17.2	2.0	74.8	<u>8.2</u>	<b>37.2</b>	<u>26.5</u>	78.0
Denoise	15.8	1.8	78.0	7.2	35.6	24.7	77.5
MFM	<u>18.5</u>	<u>2.3</u>	<u>74.2</u>	<b>9.0</b>	<u>36.9</u>	<b>26.7</b>	<b>78.5</b>

to reconstruct high-frequency components of images brings no benefits to the performance. Instead, learning high-frequency information can compensate for the ability of ViT models in capturing the high-frequency components. In contrast, our MFM outperforms its supervised counterparts in both ViT and CNN architectures as it leverages both low- and high-frequency components. Even under a demanding training procedure, *e.g.*, fine-tuning for 300 epochs (Table 4c), MFM can still improve the supervised RSB A2 baseline by 0.3% and surpass several representative contrastive-based self-supervised learning methods.

#### 4.5 Robustness Evaluation

We evaluate the robustness of our models on a series of benchmarks in three aspects: (i) adversarial robustness, (ii) common corruption robustness, and (iii) out-of-distribution robustness. For (i), we study the adversarial examples generated by white-box attackers (*e.g.*, FGSM [26] and PGD [42]) on ImageNet-1K validation set as well as natural adversarial examples on ImageNet-A [34]; for (ii), we evaluate on ImageNet-C [33] that includes 15 types of algorithmically generated corruptions with five levels of severity; for (iii), we test on ImageNet-R [32] and ImageNet-Sketch [65] that contain images with naturally occurring distribution shifts. We evaluate the same models fine-tuned on original ImageNet-1K (ViT-B/16 in Table 3 and ResNet-50 in Table 4b) without any specialized fine-tuning on the different validation sets. As shown in Table 5, we can conclude three observations: 1) Transformer-based models (*e.g.*, ViT) are more robust than the CNN counterparts (*e.g.*, ResNet-50). 2) Corruption-based tasks (*e.g.*, SR, Deblur, Denoise and MFM) are generally more robust than the MIM task (*e.g.*, MAE). 3) MFM achieves the best trade-off between standard performance and robustness (the robustness of MFM always ranks within the top two, while the standard accuracy is the best).

## 5 Conclusion and Discussion

In this work, we have studied the effectiveness of low-level image processing tasks for visual representation learning from a new frequency perspective and introduced a unified, flexible and robust self-supervised visual pre-training framework to perform image corruptions in the frequency domain. We show that without relying on mask tokens or more complex designs (*e.g.*, discrete visual tokens), a simple *mask-frequency* strategy can achieve competitive performance for both vision Transformers and convolutional neural networks. We hope our unique frequency perspective can motivate the community to rethink the role of low-level tasks for unsupervised representation learning.

**Limitations.** Our study has several limitations: 1) We mainly focus on the architectural flexibility and universality of MFM, while leaving the scaling behaviour under-explored. 2) We mainly evaluate the quality of learned representations by fine-tuning on ImageNet-1K image classification following [1], which is a more usable scenario in practice. The transferability on other downstream tasks like object detection and segmentation may need further investigation. 3) Despite the intriguing properties of the Fourier domain, the redundancy in frequencies may still exist. More advanced information suppression strategies can be further explored. We believe that our MFM can also complement recent MIM approaches to further improve the performance. We leave these explorations for future work.

**Broader impacts.** The proposed method learns statistics of the training dataset and may reflect the biases in the data. Biased measures thus have to be taken. The method may be deployed with large-scale models and data, causing negative impacts on the environment.



## Appendix

In this appendix, we provide the detailed pre-training and fine-tuning recipes in Section A. Section B provides more qualitative results including corrupted and recovered images.

### A Implementation Details

**Pre-training.** Table 6 summarizes the pre-training settings for vanilla ViT and ResNet-50 models. All experiments are conducted on 16 V100 32G GPUs for ViT models and 8 V100 32G GPUs for ResNet-50. The configurations are *shared* by different architectures, without specialized tuning. This demonstrates that MFM is *general* across architectures.

**Fine-tuning.** Table 7 and Table 8 summarize the fine-tuning settings for vanilla ViT and ResNet-50 models, respectively. The configurations for ViT are *shared* across models, except that smaller models are fine-tuned longer. The configurations for ResNet-50 basically follow [69], except that we adopt the AdamW optimizer following [24].

### B Visualization

We provide more qualitative results of corrupted images in Figure 3 following Table 2, as well as recovered images using unseen ImageNet-1K (Figure 4) and COCO (Figure 5) *validation* images.

Table 6: **Pre-training settings for vanilla ViT-S/16, ViT-B/16 and ResNet-50 models on ImageNet-1K.** Note that we adopt the *same* pre-training configurations across different architectures without further parameter tuning.

Configuration	Value
Optimizer	AdamW [41]
Pre-training epochs	300
Peak learning rate	1.2e-3
Batch size	2048
Weight decay	0.05
Optimizer momentum	$\beta_1, \beta_2 = 0.9, 0.95$ [8]
Learning rate schedule	Cosine decay
Warmup epochs	20
Gradient clipping	3.0
Dropout [58]	$\times$
Stochastic depth [36]	$\times$
LayerScale [61]	$\times$
Data augmentation	RandomResizedCrop
Pos. emb. in Transformer layers	1-D absolute pos. emb. [22]
Patch size	16
Pre-training resolution	224

Table 7: **Fine-tuning settings for vanilla ViT-S/16 and ViT-B/16 on ImageNet-1K.** We fine-tune ViT-S/16 for 200 epochs, and ViT-B/16 for 100 epochs. All other hyper-parameters are the same.

Configuration	Value
Optimizer	AdamW [41]
Fine-tuning epochs	200 (S), 100 (B)
Peak learning rate	8e-3
Layer-wise learning rate decay [1]	0.8 [14]
Batch size	2048
Weight decay	0.05
Optimizer momentum	$\beta_1, \beta_2 = 0.9, 0.999$
Learning rate schedule	Cosine decay
Warmup epochs	5
Loss function	Cross-entropy loss
Gradient clipping	$\times$
Dropout [58]	$\times$
Stochastic depth [36]	0.1
Mixup [74]	0.8
Cutmix [73]	1.0
Label smoothing [59]	0.1
Random augmentation [15]	9 / 0.5
Patch size	16
Fine-tuning resolution	224
Test resolution	224

Table 8: **Fine-tuning settings for vanilla ResNet-50 on ImageNet-1K.** The hyper-parameters generally follow [69], except that we adopt the AdamW optimizer following [24].

Configuration	100 epoch FT	300 epoch FT
Optimizer	AdamW [41]	
Peak learning rate	12e-3	
Layer-wise learning rate decay [1]	$\times$	
Batch size	2048	
Weight decay	0.02	
Learning rate schedule	Cosine decay	
Warmup epochs	5	
Loss function	Binary cross-entropy loss	
Gradient clipping	$\times$	
Dropout [58]	$\times$	
Stochastic depth [36]	$\times$	
Mixup [74]	0.1	
Cutmix [73]	1.0	
Label smoothing [59]	0.1	$\times$
Repeated augmentation [3, 35]	$\times$	$\checkmark$
Random augmentation [15]	6 / 0.5	7 / 0.5
Fine-tuning resolution	160	224
Test resolution	224	
Test crop ratio	0.95	

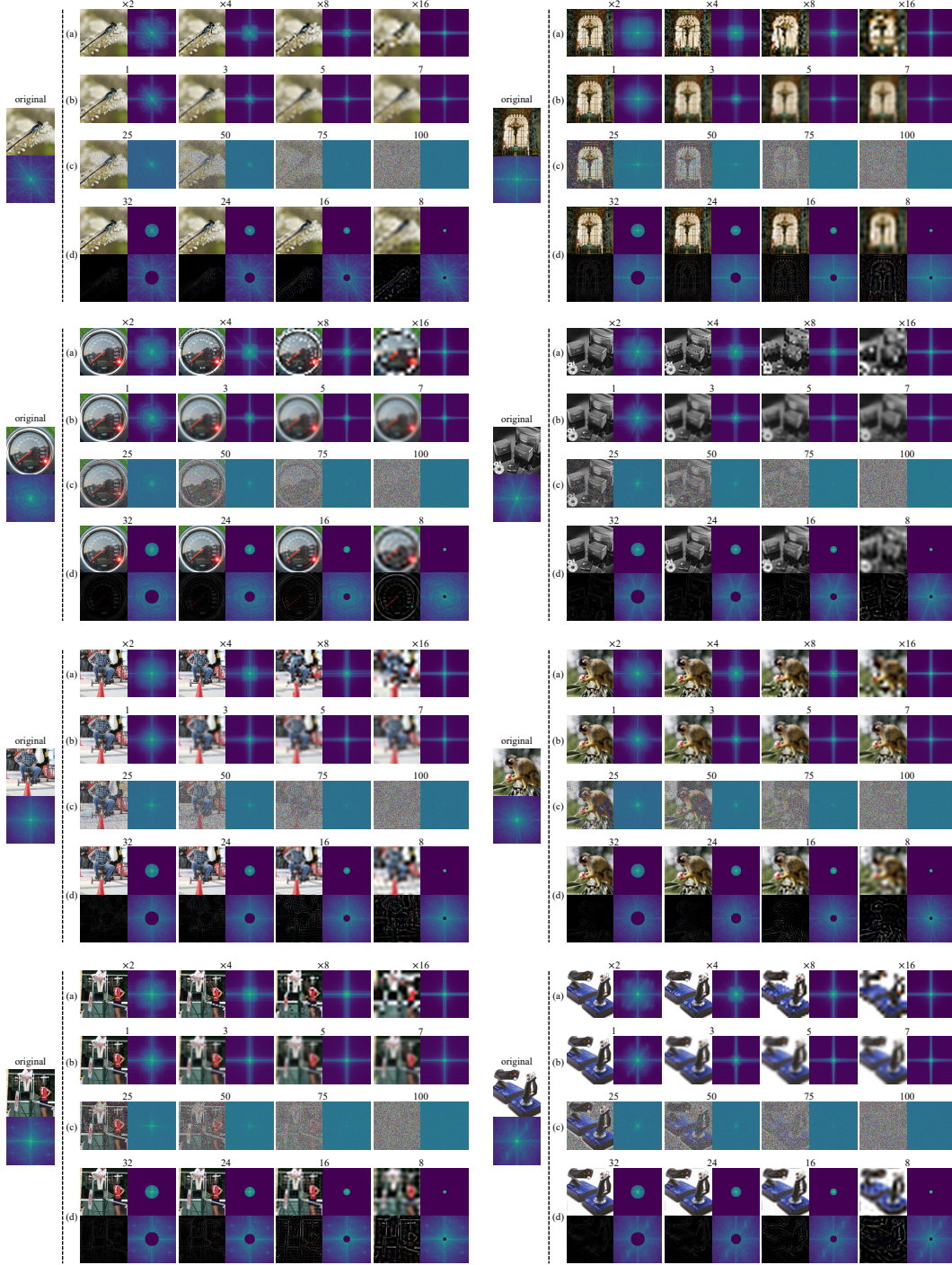


Figure 3: **More visualizations of corrupted image samples** from ImageNet-1K training set following Table 2. We visualize both images and their frequency spectrums with different degradation levels. (a) SR, (b) Deblur (kernel size 21), (c) Denoise, (d) MFM. Each task achieves its best performance with a moderate degradation intensity. See Section 4.3 for more discussion. Zoom in for best view.





Figure 4: **Example results of recovered images** on ImageNet-1K *validation* set for SR, deblurring, denoising and MFM tasks. We visualize both images and their frequency spectrums. We use the best pre-trained model of each task in Table 2 for visualization, *i.e.*, the downsampling scale factor is  $\times 8$  for SR, the Gaussian blur sigma is 5 for Deblur, the Gaussian noise sigma is 75 for Denoise, and the mask radius is 16 for MFM<sup>†</sup>. Compared with SR, Deblur and Denoise, MFM can utilize both high-frequency and low-frequency information for prediction. Zoom in for best view.

<sup>†</sup>As MFM only predicts the masked area of the frequency spectrum, we overlay the output with the visible frequency spectrum for better visual quality.

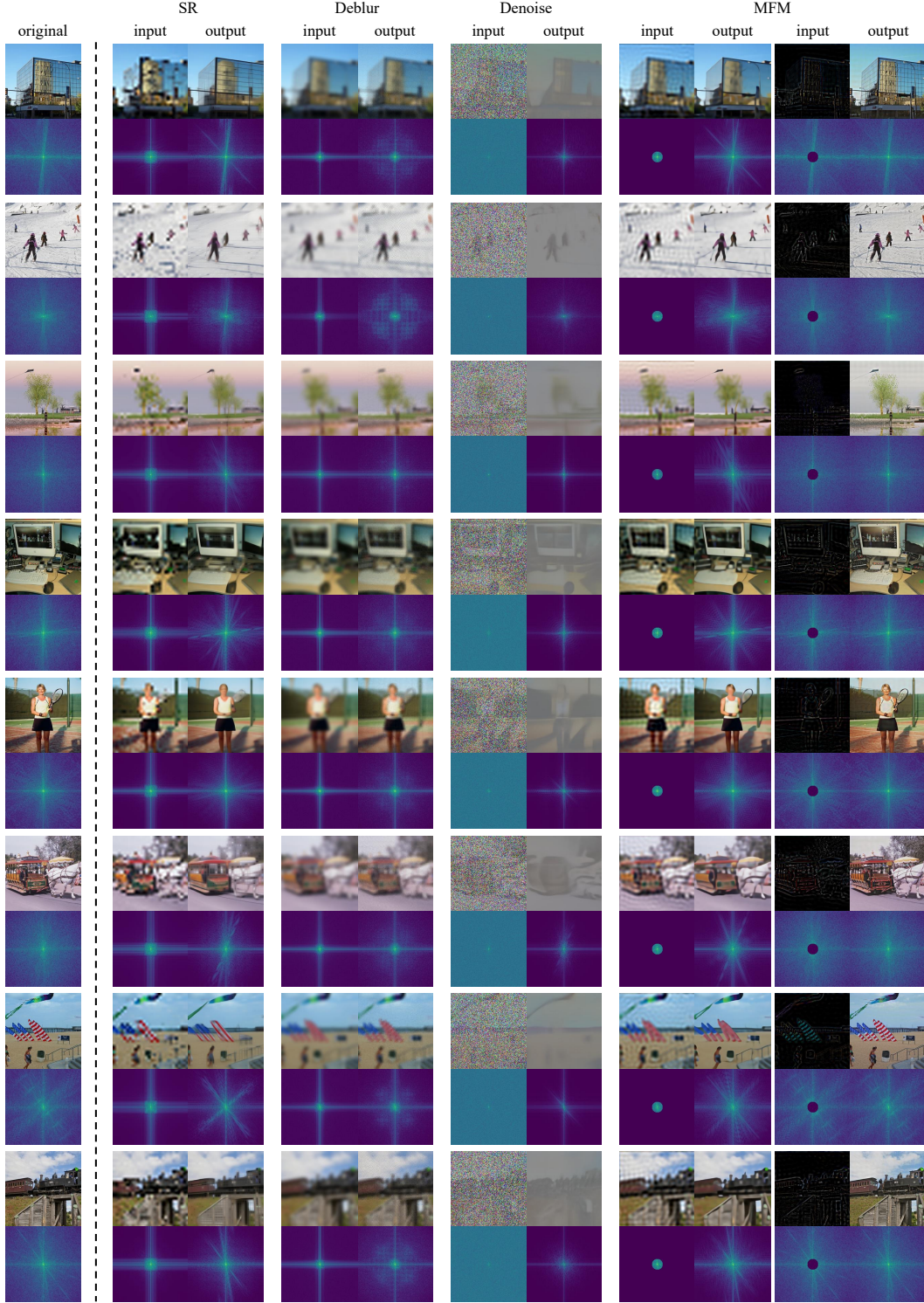


Figure 5: **Example results of recovered images** on COCO *validation* set for SR, deblurring, denoising and MFM tasks, using the models pre-trained on ImageNet-1K (the same model weights as in Figure 4). We visualize both images and their frequency spectrums. Zoom in for best view.



## References

- [1] Hangbo Bao, Li Dong, and Furu Wei. Beit: Bert pre-training of image transformers. In *ICLR*, 2022. 1, 3, 5, 6, 8, 9, 11
- [2] Irwan Bello, William Fedus, Xianzhi Du, Ekin Dogus Cubuk, Aravind Srinivas, Tsung-Yi Lin, Jonathon Shlens, and Barret Zoph. Revisiting resnets: Improved training and scaling strategies. In *NeurIPS*, 2021. 8
- [3] Maxim Berman, Hervé Jégou, Andrea Vedaldi, Iasonas Kokkinos, and Matthijs Douze. Multigrain: a unified image embedding for classes and instances. *arXiv preprint arXiv:1902.05509*, 2019. 11
- [4] Piotr Bojanowski and Armand Joulin. Unsupervised learning by predicting noise. In *ICML*, 2017. 3
- [5] Tom Brown, Benjamin Mann, Nick Ryder, Melanie Subbiah, Jared D Kaplan, Prafulla Dhariwal, Arvind Neelakantan, Pranav Shyam, Girish Sastry, Amanda Askell, et al. Language models are few-shot learners. In *NeurIPS*, 2020. 3
- [6] Mathilde Caron, Ishan Misra, Julien Mairal, Priya Goyal, Piotr Bojanowski, and Armand Joulin. Unsupervised learning of visual features by contrasting cluster assignments. In *NeurIPS*, 2020. 8
- [7] Mathilde Caron, Hugo Touvron, Ishan Misra, Hervé Jégou, Julien Mairal, Piotr Bojanowski, and Armand Joulin. Emerging properties in self-supervised vision transformers. In *ICCV*, 2021. 3, 8
- [8] Mark Chen, Alec Radford, Rewon Child, Jeffrey Wu, Heewoo Jun, David Luan, and Ilya Sutskever. Generative pretraining from pixels. In *ICML*, 2020. 3, 10
- [9] Ting Chen, Simon Kornblith, Mohammad Norouzi, and Geoffrey Hinton. A simple framework for contrastive learning of visual representations. In *ICML*, 2020. 3, 8
- [10] Xiaokang Chen, Mingyu Ding, Xiaodi Wang, Ying Xin, Shentong Mo, Yunhao Wang, Shumin Han, Ping Luo, Gang Zeng, and Jingdong Wang. Context autoencoder for self-supervised representation learning. *arXiv preprint arXiv:2202.03026*, 2022. 3
- [11] Xinlei Chen, Haoqi Fan, Ross Girshick, and Kaiming He. Improved baselines with momentum contrastive learning. *arXiv preprint arXiv:2003.04297*, 2020. 3, 8
- [12] Xinlei Chen and Kaiming He. Exploring simple siamese representation learning. In *CVPR*, 2021. 3, 8
- [13] Xinlei Chen, Saining Xie, and Kaiming He. An empirical study of training self-supervised vision transformers. In *ICCV*, 2021. 3, 8
- [14] Kevin Clark, Minh-Thang Luong, Quoc V Le, and Christopher D Manning. Electra: Pre-training text encoders as discriminators rather than generators. *arXiv preprint arXiv:2003.10555*, 2020. 6, 11
- [15] Ekin D Cubuk, Barret Zoph, Jonathon Shlens, and Quoc V Le. Randaugment: Practical automated data augmentation with a reduced search space. In *CVPRW*, 2020. 11
- [16] Jia Deng, Wei Dong, Richard Socher, Li-Jia Li, Kai Li, and Li Fei-Fei. Imagenet: A large-scale hierarchical image database. In *CVPR*, 2009. 2, 5
- [17] Jacob Devlin, Ming-Wei Chang, Kenton Lee, and Kristina Toutanova. Bert: Pre-training of deep bidirectional transformers for language understanding. In *NAACL*, 2019. 1, 3
- [18] Carl Doersch, Abhinav Gupta, and Alexei A Efros. Unsupervised visual representation learning by context prediction. In *ICCV*, 2015. 3
- [19] Piotr Dollár, Mannat Singh, and Ross Girshick. Fast and accurate model scaling. In *CVPR*, 2021. 8
- [20] Chao Dong, Chen Change Loy, Kaiming He, and Xiaoou Tang. Image super-resolution using deep convolutional networks. *TPAMI*, 2015. 3
- [21] Xiaoyi Dong, Jianmin Bao, Ting Zhang, Dongdong Chen, Weiming Zhang, Lu Yuan, Dong Chen, Fang Wen, and Nenghai Yu. Peco: Perceptual codebook for bert pre-training of vision transformers. *arXiv preprint arXiv:2111.12710*, 2021. 3
- [22] Alexey Dosovitskiy, Lucas Beyer, Alexander Kolesnikov, Dirk Weissenborn, Xiaohua Zhai, Thomas Unterthiner, Mostafa Dehghani, Matthias Minderer, Georg Heigold, Sylvain Gelly, et al. An image is worth 16x16 words: Transformers for image recognition at scale. In *ICLR*, 2020. 1, 2, 3, 5, 10
- [23] Alaaeldin El-Nouby, Gautier Izacard, Hugo Touvron, Ivan Laptev, Hervé Jégou, and Edouard Grave. Are large-scale datasets necessary for self-supervised pre-training? *arXiv preprint arXiv:2112.10740*, 2021. 3
- [24] Yuxin Fang, Li Dong, Hangbo Bao, Xinggang Wang, and Furu Wei. Corrupted image modeling for self-supervised visual pre-training. *arXiv preprint arXiv:2202.03382*, 2022. 3, 8, 10, 11
- [25] Spyros Gidaris, Praveer Singh, and Nikos Komodakis. Unsupervised representation learning by predicting image rotations. In *ICLR*, 2018. 3
- [26] Ian J Goodfellow, Jonathon Shlens, and Christian Szegedy. Explaining and harnessing adversarial examples. *arXiv preprint arXiv:1412.6572*, 2014. 9
- [27] Jean-Bastien Grill, Florian Strub, Florent Altché, Corentin Tallec, Pierre H Richemond, Elena Buchatskaya, Carl Doersch, Bernardo Avila Pires, Zhaohan Daniel Guo, Mohammad Gheshlaghi Azar, et al. Bootstrap your own latent: A new approach to self-supervised learning. In *NeurIPS*, 2020. 3, 8
- [28] Bruce C Hansen and Robert F Hess. Structural sparseness and spatial phase alignment in natural scenes. *JOSA A*, 2007. 3
- [29] Kaiming He, Xinlei Chen, Saining Xie, Yanghao Li, Piotr Dollár, and Ross Girshick. Masked autoencoders are scalable vision learners. *arXiv preprint arXiv:2111.06377*, 2021. 1, 3, 5, 8, 9

- [30] Kaiming He, Haoqi Fan, Yuxin Wu, Saining Xie, and Ross Girshick. Momentum contrast for unsupervised visual representation learning. In *CVPR*, 2020. 3
- [31] Kaiming He, Xiangyu Zhang, Shaoqing Ren, and Jian Sun. Deep residual learning for image recognition. In *CVPR*, 2016. 5, 8
- [32] Dan Hendrycks, Steven Basart, Norman Mu, Saurav Kadavath, Frank Wang, Evan Dorundo, Rahul Desai, Tyler Zhu, Samyak Parajuli, Mike Guo, et al. The many faces of robustness: A critical analysis of out-of-distribution generalization. In *ICCV*, 2021. 9
- [33] Dan Hendrycks and Thomas Dietterich. Benchmarking neural network robustness to common corruptions and perturbations. *arXiv preprint arXiv:1903.12261*, 2019. 9
- [34] Dan Hendrycks, Kevin Zhao, Steven Basart, Jacob Steinhardt, and Dawn Song. Natural adversarial examples. In *CVPR*, 2021. 9
- [35] Elad Hoffer, Tal Ben-Nun, Itay Hubara, Niv Giladi, Torsten Hoeffler, and Daniel Soudry. Augment your batch: better training with larger batches. *arXiv preprint arXiv:1901.09335*, 2019. 11
- [36] Gao Huang, Yu Sun, Zhuang Liu, Daniel Sedra, and Kilian Q Weinberger. Deep networks with stochastic depth. In *ECCV*, 2016. 10, 11
- [37] Liming Jiang, Bo Dai, Wayne Wu, and Chen Change Loy. Focal frequency loss for image reconstruction and synthesis. In *ICCV*, 2021. 3, 5
- [38] Gustav Larsson, Michael Maire, and Gregory Shakhnarovich. Learning representations for automatic colorization. In *ECCV*, 2016. 3
- [39] Yann LeCun, Bernhard Boser, John S Denker, Donnie Henderson, Richard E Howard, Wayne Hubbard, and Lawrence D Jackel. Backpropagation applied to handwritten zip code recognition. *Neural computation*, 1989. 2
- [40] Ze Liu, Yutong Lin, Yue Cao, Han Hu, Yixuan Wei, Zheng Zhang, Stephen Lin, and Baining Guo. Swin transformer: Hierarchical vision transformer using shifted windows. In *ICCV*, 2021. 3
- [41] Ilya Loshchilov and Frank Hutter. Decoupled weight decay regularization. *arXiv preprint arXiv:1711.05101*, 2017. 8, 10, 11
- [42] Aleksander Madry, Aleksandar Makelov, Ludwig Schmidt, Dimitris Tsipras, and Adrian Vladu. Towards deep learning models resistant to adversarial attacks. *arXiv preprint arXiv:1706.06083*, 2017. 9
- [43] Ishan Misra and Laurens van der Maaten. Self-supervised learning of pretext-invariant representations. In *CVPR*, 2020. 3
- [44] Mehdi Noroozi and Paolo Favaro. Unsupervised learning of visual representations by solving jigsaw puzzles. In *ECCV*, 2016. 3
- [45] Mehdi Noroozi, Hamed Pirsiavash, and Paolo Favaro. Representation learning by learning to count. In *ICCV*, 2017. 3
- [46] Henri J Nussbaumer. The fast fourier transform. In *Fast Fourier Transform and Convolution Algorithms*, pages 80–111. Springer, 1981. 4
- [47] A Oppenheim, Jae Lim, Gary Kopec, and SC Pohlig. Phase in speech and pictures. In *ICASSP*, 1979. 3
- [48] Alan V Oppenheim and Jae S Lim. The importance of phase in signals. *Proc. IEEE*, 1981. 3
- [49] Yingxue Pang, Xin Li, Xin Jin, Yaojun Wu, Jianzhao Liu, Sen Liu, and Zhibo Chen. Fan: frequency aggregation network for real image super-resolution. In *ECCV*, 2020. 3
- [50] Adam Paszke, Sam Gross, Francisco Massa, Adam Lerer, James Bradbury, Gregory Chanan, Trevor Killeen, Zeming Lin, Natalia Gimelshein, Luca Antiga, et al. Pytorch: An imperative style, high-performance deep learning library. In *NeurIPS*, 2019. 8
- [51] Deepak Pathak, Ross Girshick, Piotr Dollár, Trevor Darrell, and Bharath Hariharan. Learning features by watching objects move. In *CVPR*, 2017. 3
- [52] Deepak Pathak, Philipp Krahenbuhl, Jeff Donahue, Trevor Darrell, and Alexei A Efros. Context encoders: Feature learning by inpainting. In *CVPR*, 2016. 3
- [53] Leon N Piotrowski and Fergus W Campbell. A demonstration of the visual importance and flexibility of spatial-frequency amplitude and phase. *Perception*, 1982. 3
- [54] Alec Radford, Karthik Narasimhan, Tim Salimans, and Ilya Sutskever. Improving language understanding by generative pre-training. 2018. 3
- [55] Alec Radford, Jeffrey Wu, Rewon Child, David Luan, Dario Amodei, Ilya Sutskever, et al. Language models are unsupervised multitask learners. *OpenAI blog*, 2019. 3
- [56] Aditya Ramesh, Mikhail Pavlov, Gabriel Goh, Scott Gray, Chelsea Voss, Alec Radford, Mark Chen, and Ilya Sutskever. Zero-shot text-to-image generation. In *ICML*, 2021. 8
- [57] Yuge Shi, N Siddharth, Philip HS Torr, and Adam R Kosiorek. Adversarial masking for self-supervised learning. *arXiv preprint arXiv:2201.13100*, 2022. 3
- [58] Nitish Srivastava, Geoffrey Hinton, Alex Krizhevsky, Ilya Sutskever, and Ruslan Salakhutdinov. Dropout: a simple way to prevent neural networks from overfitting. *JMLR*, 2014. 10, 11
- [59] Christian Szegedy, Vincent Vanhoucke, Sergey Ioffe, Jon Shlens, and Zbigniew Wojna. Rethinking the inception architecture for computer vision. In *CVPR*, 2016. 11

- [60] Hugo Touvron, Matthieu Cord, Matthijs Douze, Francisco Massa, Alexandre Sablayrolles, and Hervé Jégou. Training data-efficient image transformers & distillation through attention. In *ICML*, 2021. 8, 9
- [61] Hugo Touvron, Matthieu Cord, Alexandre Sablayrolles, Gabriel Synnaeve, and Hervé Jégou. Going deeper with image transformers. In *ICCV*, 2021. 10
- [62] Hugo Touvron, Andrea Vedaldi, Matthijs Douze, and Hervé Jégou. Fixing the train-test resolution discrepancy. In *NeurIPS*, 2019. 8
- [63] Ashish Vaswani, Noam Shazeer, Niki Parmar, Jakob Uszkoreit, Llion Jones, Aidan N Gomez, Łukasz Kaiser, and Illia Polosukhin. Attention is all you need. In *NeurIPS*, 2017. 1, 5
- [64] Pascal Vincent, Hugo Larochelle, Isabelle Lajoie, Yoshua Bengio, Pierre-Antoine Manzagol, and Léon Bottou. Stacked denoising autoencoders: Learning useful representations in a deep network with a local denoising criterion. *JMLR*, 2010. 3
- [65] Haohan Wang, Songwei Ge, Zachary Lipton, and Eric P Xing. Learning robust global representations by penalizing local predictive power. In *NeurIPS*, 2019. 9
- [66] Xiaolong Wang and Abhinav Gupta. Unsupervised learning of visual representations using videos. In *ICCV*, 2015. 3
- [67] Xintao Wang, Liangbin Xie, Chao Dong, and Ying Shan. Real-esrgan: Training real-world blind super-resolution with pure synthetic data. In *ICCVW*, 2021. 7
- [68] Chen Wei, Haoqi Fan, Saining Xie, Chao-Yuan Wu, Alan Yuille, and Christoph Feichtenhofer. Masked feature prediction for self-supervised visual pre-training. *arXiv preprint arXiv:2112.09133*, 2021. 1, 3, 5
- [69] Ross Wightman, Hugo Touvron, and Hervé Jégou. Resnet strikes back: An improved training procedure in timm. *arXiv preprint arXiv:2110.00476*, 2021. 8, 9, 10, 11
- [70] Zhirong Wu, Yuanjun Xiong, Stella X Yu, and Dahua Lin. Unsupervised feature learning via non-parametric instance discrimination. In *CVPR*, 2018. 3
- [71] Zhenda Xie, Zheng Zhang, Yue Cao, Yutong Lin, Jianmin Bao, Zhuliang Yao, Qi Dai, and Han Hu. Simsim: A simple framework for masked image modeling. *arXiv preprint arXiv:2111.09886*, 2021. 1, 3, 5
- [72] Qinwei Xu, Ruipeng Zhang, Ya Zhang, Yanfeng Wang, and Qi Tian. A fourier-based framework for domain generalization. In *CVPR*, 2021. 3
- [73] Sangdoo Yun, Dongyoon Han, Seong Joon Oh, Sanghyuk Chun, Junsuk Choe, and Youngjoon Yoo. Cutmix: Regularization strategy to train strong classifiers with localizable features. In *ICCV*, 2019. 11
- [74] Hongyi Zhang, Moustapha Cisse, Yann N Dauphin, and David Lopez-Paz. mixup: Beyond empirical risk minimization. *arXiv preprint arXiv:1710.09412*, 2017. 11
- [75] Kaihao Zhang, Wenqi Ren, Wenhan Luo, Wei-Sheng Lai, Bjorn Stenger, Ming-Hsuan Yang, and Hongdong Li. Deep image deblurring: A survey. *arXiv preprint arXiv:2201.10700*, 2022. 3
- [76] Kai Zhang, Wangmeng Zuo, Yunjin Chen, Deyu Meng, and Lei Zhang. Beyond a gaussian denoiser: Residual learning of deep cnn for image denoising. *TIP*, 2017. 3
- [77] Richard Zhang, Phillip Isola, and Alexei A Efros. Colorful image colorization. In *ECCV*, 2016. 3
- [78] Richard Zhang, Phillip Isola, and Alexei A Efros. Split-brain autoencoders: Unsupervised learning by cross-channel prediction. In *CVPR*, 2017. 3
- [79] Jinghao Zhou, Chen Wei, Huiyu Wang, Wei Shen, Cihang Xie, Alan Yuille, and Tao Kong. ibot: Image bert pre-training with online tokenizer. In *ICLR*, 2022. 3, 8